Journal of Solid State Chemistry 181 (2008) 1717–1722

Contents lists available at ScienceDirect

Journal of Solid State Chemistry

journal homepage: www.elsevier.com/locate/jssc

A taxonomy of apatite frameworks for the crystal chemical design of fuel cell electrolytes

Stevin S. Pramana [a], Wim T. Klooster [a,b], Timothy J. White [a,*]

[a] Nanyang Technological University, School of Materials Science and Engineering, 50 Nanyang Avenue, Singapore 639798, Singapore
[b] Institute of Materials Research and Engineering, 3 Research Link, Singapore 117602, Singapore

ARTICLE INFO

Article history:
Received 18 January 2008
Received in revised form
19 March 2008
Accepted 22 March 2008
Available online 1 April 2008

Keywords:
Apatite
Neutron diffraction
Crystal structure
Taxonomy

ABSTRACT

Apatite framework taxonomy succinctly rationalises the crystallographic modifications of this structural family as a function of chemical composition. Taking the neutral apatite $[La_8Sr_2][(GeO_4)_6]O_2$ as a prototype electrolyte, this classification scheme correctly predicted that 'excess' oxygen in $La_9SrGe_6O_{26.5}$ is tenanted in the framework as $[La_9Sr][(GeO_4)_{5.5}(GeO_5)_{0.5}]O_2$, rather than the presumptive tunnel location of $[La_9Sr][(GeO_4)_6]O_{2.5}$. The implication of this approach is that in addition to the three known apatite genera—$\boldsymbol{A_{10}(BO_3)_6X_2}$, $\boldsymbol{A_{10}(BO_4)_6X_2}$, $\boldsymbol{A_{10}(BO_5)_6X_2}$—hybrid electrolytes of the types $\boldsymbol{A_{10}(BO_3/BO_4/BO_5)_6X_2}$ can be designed, with potentially superior low-temperature ion conduction, mediated by the introduction of oxygen to the framework reservoir.

1. Introduction

Solid oxide fuel cells will be a core technology of the hydrogen economy and a key component of these devices is an electrolytic membrane separating air on the cathode side from fuel (H_2) at the anode [1–3]. The electrolyte is insulating to force electrons through the external circuit, but additionally and more critically, must readily transport oxygen ions across the membrane. Many ceramic electrolytes are under consideration including zirconia and perovskites but these operate at relatively high temperatures (>700 °C) to achieve acceptable ion fluxes, and such conditions can lead to the failure of membrane seals [4–7]. Germanates and silicates of the apatite family display high ionic conductivity at a relatively modest 500 °C [8–12], however, the precise mode of ion migration and the role of nonstoichiometry and chemical enhancers, such as transition metals, has remained elusive. A recent revision of the crystal structure of the prototypical electrolyte apatite $[La_{10}][(GeO_4)_5(GeO_5)]O_2$ showed that 'interstitial' oxygen was located primarily in the walls of a zeolite-like framework [13], rather than in the conducting channels as conventionally assumed [14–20]. Here we integrate this revised structure within the broader context of apatite crystal chemistry to devise a succinct, yet comprehensive, classification of framework adaptation in these materials. The utility of this new taxonomy for electrolyte design is demonstrated through the prediction and direct observation of the controlled partitioning of 'excess' oxygen ions to the framework reservoir in $[La_{10-x}Sr_x][(GeO_4)_{5+x/2}(GeO_5)_{1-x/2}]O_2$ apatites.

2. Apatite framework taxonomy

Hydroxyapatite ($Ca_{10}(PO_4)_6(OH)_2$) (HAp) is familiar as the idealised inorganic component of bone and teeth [21]. The architecture of HAp is zeolitic [22]. It is constructed from columns of CaO_6 metaprisms (a distorted trigonal prism) hinged by isolated PO_4 tetahedra to create a framework of ideal stoichiometry $[Ca_4(PO_4)_6]^{10-}$ that circumscribes one-dimensional channels containing $[Ca_6(OH)_2]^{10+}$ (Fig. 1). Many chemical analogues adopt this structural motif and counter-ions of valences 1+ to 7+ can be incorporated to maintain charge neutrality while the framework flexes topologically to match the tunnel diameter with the abundance and size of its contents.

More than 70 apatite chemical endmembers are known whose compositions can be generalised as $\boldsymbol{A_{10}(BO_4)_6X_2}$ where *A* and *B* are larger and smaller cations and *X* are anions [22,23]. This genus is usually considered the only representative of the apatite family, but in fact, the framework is exceedingly adaptive (Fig. 2). Mimetite is a mineral species with ideal composition $Pb_{10}(AsO_4)_6Cl_2$ [24], but unlike HAp where *B* is of fixed valence (P^{5+}), arsenic may be reduced from As^{5+} to As^{3+}, and the $(AsO_4)^{3-}$ tetrahedra replaced by $(AsO_3)^{3-}$. When reduction proceeds to completion the distinct species $Pb_{10}(AsO_3)_6Cl_2$ finnemanite crystallises [25,26], where $[Pb_4(AsO_3)_6]^{10-}$ and $[Pb_6Cl_2]^{10+}$ are

* Corresponding author. Fax: +65 6790 9081.
E-mail address: tjwhite@ntu.edu.sg (T.J. White).

0022-4596/$ - see front matter © 2008 Elsevier Inc. All rights reserved.
doi:10.1016/j.jssc.2008.03.028

the framework and tunnel components, respectively. Although fully six oxygens are removed per formula unit the structure remains intact through the stabilising effects of the stereochemically active lone pair electrons of As^{3+} and Pb^{2+}. Finnemanite can be considered the archetype of the $\boldsymbol{A_{10}(BO_3)_6X_2}$ apatite genus. Finally, oxidised apatites result from the introduction of intermetallic species at the *B*-position. One example is $Sr_{10}(ReO_5)_6Cl_2$ where Re^{7+} is accommodated in BO_5 square pyramidal coordination rather than BO_4 tetrahedra resulting in an $[Sr_4(ReO_5)_6]^{10-}$ framework and $[Sr_6Cl_2]^{10+}$ tunnel contents [27]. About 10 compounds, all rhenates and osmates, belong to the $\boldsymbol{A_{10}(BO_5)_6X_2}$ genus [22,23].

All three apatite genera are hettotypes derived from $P6_3/mcm$ symmetry that describes the structure of many alloys [28], including $Ca_{10}As_6$, which has an atomic arrangement equivalent to that of mimetite and finnemanite. This common descent of apatites as anion-stuffed alloys not only allows for systematic classification, but also predicates feasible stoichiometries and chemical tailoring of functionality. Moreover, there is in principle no impediment to the creation of apatite hybrids that contain mixtures of BO_3, BO_4, and BO_5 framework elements, as only the oxygen sub-structure is modified without disturbing the cation array. One such hybrid appears when carbonate (CO_3^{2-}) is incorporated in dental enamel and the apatites $[Ca_{10-x}Na_x][(PO_4)_{6-x}(CO_3)_x](OH)_2$ have been synthesised where there is partial replacement of the $(PO_4)^{3-}$ group by $(CO_3)^{2-}$. In this case, charge balance is maintained through the introduction of Na^+ as a framework counter ion by the substitution $Ca^{2+}+(PO_4)^{3-} \rightarrow Na^+ + (CO_3)^{2-}$ [29]. Another hybrid of this type may participate in the phase transition of mimetite to clinomimetite at ~100 °C through the partial reduction of As^{5+} and the inclusion of finnemanite components [24]. Thus, hybrid apatites of the type $\boldsymbol{A_{10}(BO_4)_{6-x}(BO_3)_xX_2}$ exist.

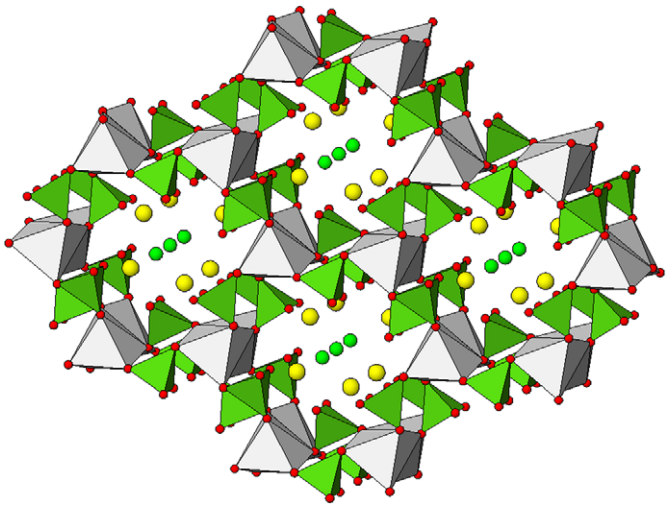

Fig. 1. Tunnel structure of the $A_{10}(BO_4)_6X_2$ apatite genus exemplified by the electrolyte $[La_8Sr_2][(GeO_4)_6]O_2$. The grey AO_6 polyhedra are metraprisms containing lanthanum and strontium while the green BO_4 tetrahedra accommodate germanium. The tunnels contain the remaining lanthanum (yellow) and oxygen (green). The stoichiometry of the framework is $[A_4(BO_4)_6]$ while the large tunnels retain $[A_6X_2]$.

Hybrids containing mixtures of BO_4/BO_5 units were unknown before the recognition that $[La_{10}][(GeO_4)_5(GeO_5)]O_2$ electrolyte apatite contains germanium in both tetrahedral and trigonal bipyramidal coordination to yield a $[La_4(GeO_4)_5(GeO_5)]^{14-}$ framework surrounding $[La_6O_2]^{14+}$ [13]. This surprising result—it had been thought extra-stoichiometric oxygen was retained in the tunnels rather than the framework—is the first example of an $\boldsymbol{A_{10}(BO_4)_{6-x}(BO_5)_xX_2}$ compound. From this study, a picture emerged of an electrolyte with a framework reservoir feeding oxygen ions into the larger tunnels where they can rapidly migrate; this new model also accounted for the overlooked phenomenon of substantial oxygen transport across, as well as along, the tunnels [30]. The implication is that apatite electrolyte performance is mediated not by the concentration of oxygen ions within the conducting tunnels, but the storage capacity of the framework that can both charge the conduit with O^{2-}, and at the unit cell scale, circumvent tunnel blockages by inter-tunnel diffusion.

Finally, while $\boldsymbol{A_{10}(BO_5)_{6-x}(BO_3)_xX_2}$ hybrids have not yet been reported, we can speculate that derivatives of $Sr_{10}(ReO_5)_6Cl_2$ such as $[Sr_{10-x}Na_x][(ReO_5)_{6-x}(CO_3)_x]Cl_2$, where $Sr^{2+}+(ReO_5)^{3-} \rightarrow Na^+ + (CO_3)^{2-}$ might be prepared and exhibit interesting electrolyte properties.

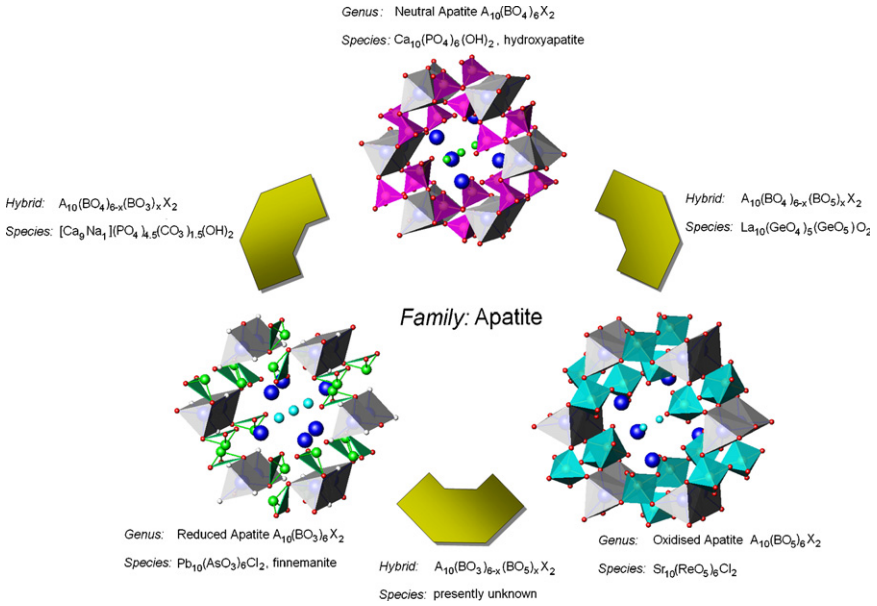

Fig. 2. The apatite crystallographic family. In this taxonomy the apatite frameworks are divided into three genera: neutral apatites containing only (BO_4) tetrahedra, reduced apatites made up of (BO_3) units, and oxidised apatites with (BO_5) polyhedra. Hybrid apatites composed of mixtures of $BO_3/BO_4/BO_5$ provide a means for crystallochemically tailoring the functionality of apatites.

Table 1
Crystal chemical data for apatite electrolytes

Parameter	Composition		
	$La_{10}Ge_6O_{27}$ $x=0$	$La_9SrGe_6O_{26.5}$ $x=1$	$La_8Sr_2Ge_6O_{26}$ $x=2$
Space group	$P\bar{1}$	$P\bar{1}$	$P6_3/m$
a (Å)	9.9346(7)	9.875(2)	9.9047(2)
b (Å)	9.9132(7)	9.893(2)	9.9047(2)
c (Å)	7.3021(5)	7.308(1)	7.3138(2)
α (deg)	90.960(5)	89.90(3)	90
β (deg)	88.079(5)	89.59(2)	90
γ (deg)	120.890(4)	119.96(2)	120
Volume (Å^3)	616.79(8)	618.5(2)	621.38(3)
Framework	$[La_4(GeO_4)_5(GeO_5)]^{14-}$	$[(La_3Sr)(GeO_4)_{5.5}(GeO_5)_{0.5}]^{14-}$	$[(La_2Sr_2)(GeO_4)_6]^{14-}$
Tunnel	$[La_6O_2]^{14+}$	$[La_6O_2]^{14+}$	$[La_6O_2]^{14+}$

3. Experimental

$La_{10-x}Sr_xGe_6O_{27-x/2}$ ($x=0$, 1, 2) were synthesised by solid-state reaction.

$$(5-x/2)\ La_2O_3 + xSrCO_3 + 6GeO_2 \rightarrow La_{10-x}Sr_xGe_6O_{27-x/2} + xCO_2$$

La_2O_3 (BDH, 99.5%), $SrCO_3$ (Riedel-de Haën, 96%), GeO_2 (Alfa Aesar, 99.999%) were dehydrated for 4 h at 1000, 500, 600 °C, respectively, after which stoichiometric amounts were manually ground in an agate mortar and pestle and calcined at 1100 °C for 16 h. These powders were reground and sintered at 1300 °C for another 16 h in a platinum crucible.

Powder neutron diffraction data were collected on the high-resolution powder diffractometer (HRPD) at the high flux Australian reactor (HIFAR) operated by the Australian Nuclear Science and Technology Organisation (ANSTO). Approximately 15 g of the apatite was loaded into a 12 mm diameter vanadium can that was rotated during data collection. The diffraction data were accumulated at ambient temperature using a neutron wavelength of 1.4925(1) Å from 0.027° to 150.027° 2θ in 0.05° steps.

The crystal structure of $La_{10-x}Sr_xGe_6O_{27-x/2}$ ($x=0$, 1, 2) were refined by Rietveld analysis using data from 9° to 150° in 2θ with a pseudo-Voigt peak shape profile as implemented in *TOPAS* [31], and a starting model using the atomic positions of $La_{10}(GeO_4)_5(GeO_5)O_2$ in $P\bar{1}$ [13], although for $x=2$ the higher symmetry $P6_3/m$ was most satisfactory. Difference-Fourier maps were generated using *GFOURIER* [32] embedded in *FULLPROF* [33]. For each data set, a five-coefficient Chebychev polynomial and $1/x$ background, a zero error, unit cell parameters, scale factors and crystal size were refined sequentially. Neutron scattering lengths of 0.824, 0.702, 0.81929, and 0.5803×10^{-12} cm were used for La, Sr, Ge, and O, respectively [34]. The cation positions were refined first, followed by the oxygen positions. For $La_9SrGe_6O_{26.5}$ and $La_{10}Ge_6O_{27}$, the Ge(3) tetrahedron was modelled with disordered positions and isotropic temperature displacement factors for all atoms were refined in groups as La1/La2 (framework cations); La3/La4/La5 (tunnel cations); all Ge; and all O were constrained to have the same value. The anion at the centre of the tunnel (O13) was treated separately when refining the thermal vibration.

4. Results

At one compositional extreme is $[La_{10}][(GeO_4)_5(GeO_5)]O_2$ the partially oxidised hybrid, while at the other is the neutral apatite $[La_8Sr_2][(GeO_4)_6]O_2$, leaving unresolved the location and abundance of interstitial oxygen in the intermediate apatite $La_9SrGe_6O_{26.5}$. All samples synthesised were single phase within the detection limit of neutron diffraction data. The $x=2$ compound is of higher symmetry (hexagonal $P6_3/m$) than $x=0$ and 1 (triclinic $P\bar{1}$) materials, however, the departure from the hexagonal metric is quite small (Table 1). As strontium displaces lanthanum the unit cell dilates because the effective ionic radius of Sr^{2+} (1.26 Å for VIII coordination) is larger than La^{3+} (1.16 Å) [35].

The $x=2$ neutral apatite $[La_8Sr_2][(GeO_4)_6]O_2$ is isostructural with HAp. All the strontium atoms partition to the framework with the tunnel sites solely occupied by lanthanum, and consequently, the complete crystallochemical formula can be expressed as $[La_2Sr_2][La_6][(GeO_4)_6]O_2$.[1] As expected, nuclear density mapping provided no evidence of excess oxygen within the tunnels or framework (Fig. 3a). In contrast, the oxidised apatite with $x=0$ contains additional oxygen to balance the replacement of strontium by trivalent lanthanum ($2Sr^{2+}+V_O^{2-}\rightarrow 2La^{3+}+O^{2-}$). These oxygen (designated O14) are clearly evident in the nuclear density map (Fig. 3c) and located in the framework at the fractional co-ordinates $\pm[0.028(4), 0.477(4), 0.511(5)]$ with an occupancy of 0.5. The 'interstitial' oxygen converts one-sixth of the GeO_4 tetrahedra to GeO_5 trigonal bipyamids, and this apatite is represented as $[La_{10}][(GeO_4)_5(GeO_5)]O_2$ [13]. According to framework taxonomy it is predicted that the additional oxygen in the intermediate apatite $La_9SrGe_6O_{26.5}$ ($x=1$) will be tenanted entirely in the channel walls as $[La_9Sr][(GeO_4)_{5.5}(GeO_5)_{0.5}]O_2$ rather than occupy the tunnel as $[La_9Sr][(GeO_4)_6]O_{2.5}$. A combination of nuclear density mapping and structure refinement confirmed this presumption with the interstitial oxygen (also O14) positioned at $\pm[0.02(2), 0.45(2), 0.50(2)]$ with an occupancy of 0.25 (Tables 2 and 3, Figs. 3b and 4). In this case, the five-coordinate Ge polyhedron is best described as a square pyramid (GeO_5) (Fig. 5). The Ge1–O4 bond distance is rather short (1.45(4)Å), however, the Ge bond-valence sum gives 4.02 v.u. for this very distorted tetrahedron. Taken together, these results confirm that limited extra-stoichiometric oxygen can reside within the tunnels due to bond-valence constraints, while there is a strong preference for 'interstitial' oxygen to concentrate within the framework.

5. Discussion

It has previously been shown that superior oxygen conductivity is achieved by light doping ($x\leqslant0.5$) of $[La_{10-x}Sr_x][(GeO_4)_{5+x/2}(GeO_5)_{1-x/2}]O_2$ with strontium, however, the origin of the enhanced conductivity could not then be addressed [36]. It now

[1] Further details of the crystal structure investigations may be obtained from the Fachinformationszentrum Karlsruhe, 76344 Eggenstein-Leopoldshafen, Germany (Fax: +49 7247 808 666; e-mail: crysdata@fiz-karlsruhe.de) on quoting the deposition numbers CSD-418708 and CSD-418709).

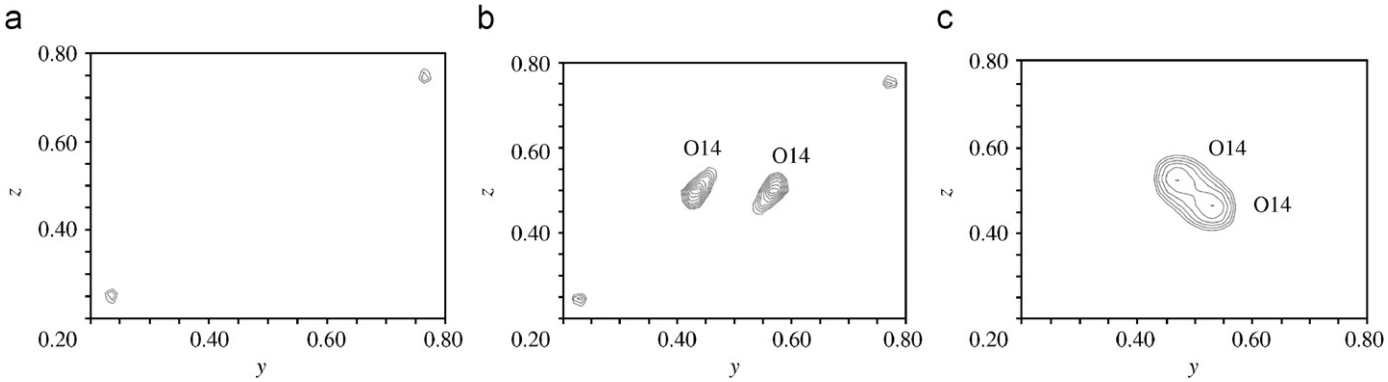

Fig. 3. Nuclear density maps of the regions where framework interstitial atoms appear for (a) $[La_8Sr_2][(GeO_4)_6]O_2$, (b) $[La_9Sr][(GeO_4)_{5.5}(GeO_5)_{0.5}]O_2$, and (c) $[La_{10}][(GeO_4)_5(GeO_5)]O_2$. The concentration of extra-stoichiometric oxygen increases with higher La^{3+} content to achieve charge balance. Similar mapping around the tunnel-centre where excess oxygen is normally presumed resident did not reveal additional atoms. The slight shifts in O14 convert the GeO_5 trigonal bipyramids in $[La_{10}][(GeO_4)_5(GeO_5)]O_2$ to square pyramids in $[La_9Sr][(GeO_4)_{5.5}(GeO_5)_{0.5}]O_2$.

Table 2
Unit cell parameters, fractional atomic coordinates, occupancies and isotropic thermal displacements of $[La_9Sr][(GeO_4)_{5.5}(GeO_5)_{0.5}]O_2$

R_{wp}[a]	0.097	a (Å)	9.875(2)
S_{wp}	0.6	b (Å)	9.893(2)
R_b	0.018	c (Å)	7.308(1)
Number of reflections	2796	α (deg)	89.90(3)
Number of parameters	101	β (deg)	89.59(2)
Neutron wavelength (Å)	1.4925(1)	γ (deg)	119.96(2)
		V (Å^3)	618.5(2)

Atom	x	y	z	Occupancy	B (Å^2)
La/Sr1	0.333(4)	0.675(5)	0.009(5)	0.75/0.25	1.0(3)
La/Sr2	0.300(3)	0.645(5)	0.502(4)	0.75/0.25	1.0(3)
La3	0.232(4)	0.991(3)	0.241(5)	1	0.7(2)
La4	0.012(3)	0.227(3)	0.246(5)	1	0.7(2)
La5	0.742(3)	0.763(4)	0.245(4)	1	0.7(2)
Ge1	0.423(3)	0.378(3)	0.251(4)	1	0.1(2)
Ge2	0.629(3)	0.027(3)	0.260(4)	1	0.1(2)
Ge3	0.996(4)	0.617(5)	0.249(6)	0.75	0.1(2)
Ge3a	0.92(1)	0.59(1)	0.30(1)	0.25	0.1(2)
O1	0.296(5)	0.487(5)	0.251(7)	1	0.3(1)
O2	0.521(5)	0.840(4)	0.264(6)	1	0.3(1)
O3	0.185(6)	0.705(6)	0.253(8)	0.75	0.3(1)
O3a	0.14(2)	0.64(2)	0.21(2)	0.25	0.3(1)
O4	0.592(4)	0.470(5)	0.255(7)	1	0.3(1)
O5	0.529(5)	0.145(5)	0.245(6)	1	0.3(1)
O6	0.882(7)	0.387(6)	0.224(7)	0.75	0.3(1)
O6a	0.78(2)	0.34(2)	0.23(2)	0.25	0.3(1)
O7	0.346(5)	0.252(5)	0.056(4)	1	0.3(1)
O8	0.787(4)	0.080(5)	0.095(5)	1	0.3(1)
O9	0.904(5)	0.656(5)	0.077(5)	1	0.3(1)
O10	0.680(5)	0.777(4)	0.532(5)	1	0.3(1)
O11	0.251(6)	0.916(6)	0.560(6)	1	0.3(1)
O12	0.058(6)	0.351(6)	0.555(8)	0.75	0.3(1)
O12a	0.01(2)	0.24(1)	0.59(2)	0.25	0.3(1)
O13	0.990(6)	0.997(6)	0.257(8)	1	0.5(5)
O14	0.02(2)	0.45(2)	0.50(2)	0.25	0.3(1)

[a] Agreement measures are $R_{wp} = [(\Sigma_i w_i|y_{io}-y_{ci}|^2)/\Sigma_i w_i y_{io}^2]^{1/2}$, $S_{wp} = R_{wp}/R_{exp}$ and $R_b = \Sigma_i|I_{ko}-I_{kc}|/\Sigma_i I_{ko}$.

appears that slightly sub-stoichiometric oxidised apatites provide facile pathways to inject oxygen into the conducting channels. Fully stoichiometric $[La_{10}][(GeO_4)_5(GeO_5)]O_2$ apatite, while a substantially better ion conductor than the neutral apatite $[La_8Sr_2][(GeO_4)_6]O_2$, is less disposed to release oxygen into the channel than oxidised strontian compounds because of the limited availability of empty interstitial sites to accommodate transitory O^{2-} ions [9,37].

Although additional conductivity measurements and atomistic simulations correlated with structural analysis are required, this study provides guidance for the design of apatite electrolytes. It is common practice to introduce oxygen by replacing large divalent *A*-cations (e.g. Ca, Sr, Ba) with trivalent rare-earth elements, but such syntheses can yield cation-deficient apatites such as $La_{9.33}(GeO_4)_6O_2$ whose ion fluxes are not optimal. Less attention has been paid to the use of transition metals [37,38], but their incorporation can enhance conduction [39], and Mössbauer spectroscopy of $La_{10}Si_5FeO_{26.5}$ was consistent with partial conversion of iron tetrahedra to 5 coordination [40], so that this electrolyte should be described as $[La_{10}][(SiO_4)_5(Fe^{3+}O_4)_{0.5}$

Table 3
Selected bond distances (Å) for $[La_9Sr][(GeO_4)_{5.5}(GeO_5)_{0.5}]O_2$

La1–O6a	2.1(2)	La5–O10	2.20(4)
La1–O3a	2.3(2)	La5–O7	2.35(4)
La1–O3	2.41(6)	La5–O13	2.39(4)
La1–O1	2.45(5)	La5–O4	2.51(4)
La1–O5	2.45(4)	La5–O9	2.62(6)
La1–O6	2.56(6)	La5–O2	2.65(6)
La1–O2	2.57(4)	La5–O12a	2.8(2)
La1–O4	2.71(5)	La5–O12	3.10(7)
La1–O7	2.91(5)	La5–O8	3.14(5)
La1–O9	2.99(4)	Average	2.64
Average	2.55		
		Ge1–O1	2.02(6)
La2–O6a	2.1(2)	Ge1–O4	1.45(4)
La2–O3	2.39(8)	Ge1–O7	1.79(3)
La2–O1	2.39(5)	Ge1–O10	2.08(4)
La2–O14	2.5(1)	Average	1.84
La2–O6	2.59(7)		
La2–O3a	2.6(2)	Ge2–O2	1.62(3)
La2–O4	2.61(7)	Ge2–O5	1.86(6)
La2–O5	2.67(5)	Ge2–O8	1.82(4)
La2–O2	2.69(4)	Ge2–O11	1.68(5)
La2–O12	2.71(6)	Average	1.75
La2–O14	2.8(2)		
La2–O11	2.99(7)	Ge3–O3	1.62(7)
Average	2.59	Ge3–O6	1.98(7)
		Ge3–O9	1.71(7)
La3–O13	2.41(8)	Ge3–O12	1.61(8)
La3–O11	2.48(5)	Average	1.73
La3–O8	2.54(4)		
La3–O5	2.55(5)	Ge3a–O3a	2.12(21)
La3–O12a	2.6(1)	Ge3a–O6a	2.25(16)
La3–O10	2.61(4)	Ge3a–O9	1.77(10)
La3–O7	2.61(5)	Ge3a–O12a	1.68(16)
La3–O3	2.63(7)	Ge3–O14	1.74(19)
La3–O3a	3.2(2)	Average	1.91
Average	2.63		
		Split sites	
La4–O13	2.19(6)	Ge3–Ge3a	0.78(12)
La4–O8	2.26(3)	O3–O3a	0.67(14)
La4–O6	2.49(8)	O6–O6a	0.87(15)
La4–O12a	2.5(1)	O12–O12a	1.03(14)
La4–O12	2.51(6)		
La4–O9	2.57(4)		
La4–O11	2.65(5)		
La4–O1	2.70(4)		
La4–O14	2.9(2)		
La4–O6a	3.0(2)		
Average	2.58		

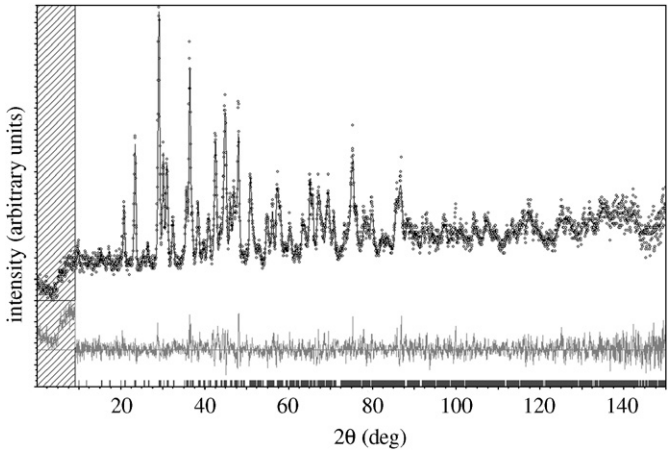

Fig. 4. Rietveld plot of the neutron diffraction data of $[La_9Sr][(GeO_4)_{5.5}(GeO_5)_{0.5}]O_2$ collected at room temperature. The observed intensity data are shown by dots, with the solid line representing the calculated intensity. Differences between observed and calculated intensities are plotted beneath. Vertical markers indicate the Bragg reflections.

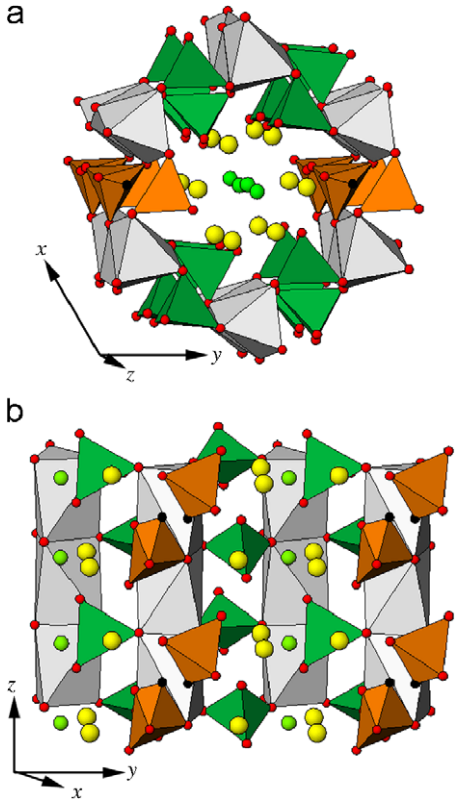

Fig. 5. Clinographic projections of $[La_9Sr][(GeO_4)_{5.5}(GeO_5)_{0.5}]O_2$ along the (a) [001] and (b) [100] directions. The GeO_4 tetrahedra and GeO_5 square pyramids are shown in green and brown, respectively, while the LaO_6 metaprisms are grey. The green atoms are tunnel oxygens. The extra-stoichiometric oxygen sites (black) in the framework are partially tenanted and occupied on average 25% of the time.

$(Fe^{3+}O_5)_{0.5}]O_2$. Indeed, the introduction of smaller cations such as Al^{3+} and B^{3+} which favour penta-coordination generally improves conduction [37]. It may be feasible to regulate elevated oxygen levels through the addition of highly oxidised *B*-cations such as Re^{7+}. For example, doping $[La_{10}][(GeO_4)_5(GeO_5)]O_2$ according to the coupled substitution $La^{3+}+(GeO_4)^{4-} \rightarrow Ba^{2+}+(ReO_5)^{3-}$ could produce the hybrid apatites $[La_{10-x}Ba_x][(GeO_4)_{5-x}(ReO_5)_x(GeO_5)]O_2$ with potentially superior control of oxygen content during synthesis and higher conductivity even at low rhenium levels.

6. Conclusions

It will be the task of future research to exploit these design concepts, which do not supersede those methods that more directly manipulate tunnel anion content in apatites, but advise that due consideration be given to chemical tailoring that enhances oxygen mobility both through the framework walls and along the conducting channels in low-temperature solid oxide fuel cell electrolytes. This new taxonomy can also guide the design of medical apatites (such as zincian HAp-coated prostheses to enhance bone growth), catalytic apatites for pollution abatement, and nuclear waste form apatites.

References

[1] R. Bove, S. Ubertini, J. Power Sources 159 (2006) 543.
[2] N.P. Brandon, S. Skinner, B.C.H. Steele, Annu. Rev. Mater. Res. 33 (2003) 183.
[3] N.Q. Minh, Solid State Ionics 174 (2004) 271.
[4] J.W. Fergus, J. Power Sources 162 (2006) 30.

[5] V.V. Kharton, F.M.B. Marques, A. Atkinson, Solid State Ionics 174 (2004) 135.
[6] D.W. Strickler, W.G. Carlson, J. Am. Ceram. Soc. 47 (1964) 122.
[7] J.W. Stevenson, T.R. Armstrong, D.E. McCready, L.R. Pederson, W.J. Weber, J. Electrochem. Soc. 144 (1997) 3613.
[8] P.R. Slater, J.E.H. Sansom, Solid State Phenom. 90–91 (2003) 195.
[9] P.R. Slater, J.E.H. Sansom, J.R. Tolchard, Chem. Rec. 4 (2004) 373.
[10] E.J. Abram, C.A. Kirk, D.C. Sinclair, A.R. West, Solid State Ionics 176 (2005) 1941.
[11] S. Nakayama, T. Kageyama, H. Aono, Y. Sadaoka, J. Mater. Chem. 5 (1995) 1801.
[12] S. Nakayama, H. Aono, Y. Sadaoka, Chem. Lett. 24 (1995) 431.
[13] S.S. Pramana, W.T. Klooster, T.J. White, Acta Crystallogr. B 63 (2007) 597.
[14] J.R. Tolchard, M.S. Islam, P.R. Slater, J. Mater. Chem. 13 (2003) 1956.
[15] L. León-Reina, E.R. Losilla, M. Martínez-Lara, S. Bruque, M.A.G. Aranda, J. Mater. Chem. 14 (2004) 1142.
[16] L. León-Reina, J.M. Porras-Vázquez, E.R. Losilla, M.A.G. Aranda, Solid State Ionics 177 (2006) 1307.
[17] L. León-Reina, E.R. Losilla, M. Martínez-Lara, S. Bruque, A. Llobet, D.V. Sheptyakov, M.A.G. Aranda, J. Mater. Chem. 15 (2005) 2489.
[18] Y. Masubuchi, M. Higuchi, T. Takeda, S. Kikkawa, Solid State Ionics 177 (2006) 263.
[19] H. Okudera, Y. Masubuchi, S. Kikkawa, A. Yoshiasa, Solid State Ionics 176 (2005) 1473.
[20] L. León-Reina, M.C. Martín-Sedeño, E.R. Losilla, A. Cabeza, M. Martínez-Lara, S. Bruque, F.M.B. Marques, D.V. Sheptyakov, M.A.G. Aranda, Chem. Mater. 15 (2003) 2099.
[21] M.I. Kay, R.A. Young, Nature 204 (1964) 1050.
[22] T. White, C. Ferraris, J. Kim, S. Madhavi, in: G. Ferraris, S. Merlino (Eds.), Reviews in Mineralogy and Geochemistry, vol. 57, Mineralogy Society of America, Washington, DC, 2005, p. 307.
[23] T.J. White, D. ZhiLi, Acta Crystallogr. B 59 (2003) 1.
[24] Y.-S. Dai, J.M. Hughes, P.B. Moore, Can. Mineral. 29 (1991) 369.
[25] H. Effenberger, F. Pertlik, Tschermaks Mineral. Petrogr. Mitt. 26 (1979) 95.
[26] T. Baikie, C. Ferraris, W.T. Klooster, S. Madhavi, S.S. Pramana, A. Pring, G. Schmidt, T.J. White, Acta Crystallogr. B 64 (2008) 34.
[27] P.J.-P. Besse, G. Baud, G. Levasseur, R. Chevalier, Acta Crystallogr. B 35 (1979) 1756.
[28] A. Vegas, M. Jansen, Acta Crystallogr. B 58 (2002) 38.
[29] H.E. Feki, J.M. Savariault, A.B. Salah, J. Alloys Compd. 287 (1999) 114.
[30] S. Nakayama, M. Higuchi, J. Mater. Sci. Lett. 20 (2001) 913.
[31] Bruker, TOPAS Version 3, Bruker AXS Inc., Madison, WI, USA, 2005.
[32] J. Gonzales-Platas, J. Rodriguez-Carvajal, GFOURIER Version 04.05, 04.05, Universidad de la Laguna, Tenerife, Spain, 2006.
[33] J. Rodriguez-Carvajal, FULLPROF Version 3.5d, 1990.
[34] V.F. Sears, in: A.J.C. Wilson (Ed.), International Tables for Crystallography, vol. C, Kluwer Academic Publishers, Dordrecht, 1993, p. 383.
[35] R. Shannon, Acta Crystallogr. A 32 (1976) 751.
[36] H. Arikawa, H. Nishiguchi, T. Ishihara, Y. Takita, Solid State Ionics 136–137 (2000) 31.
[37] E. Kendrick, M.S. Islam, P.R. Slater, J. Mater. Chem. 17 (2007) 3104.
[38] J.R. Tolchard, P.R. Slater, M.S. Islam, Adv. Funct. Mater. 17 (2007) 2564.
[39] J. McFarlane, S. Barth, M. Swaffer, J. Sansom, P. Slater, Ionics 8 (2002) 149.
[40] V.V. Kharton, A.L. Shaula, M.V. Patrakeev, J.C. Waerenborgh, D.P. Rojas, N.P. Vyshatko, E.V. Tsipis, A.A. Yaremchenko, F.M.B. Marques, J. Electrochem. Soc. 151 (2004) A1236.